Applied Catalysis B: Environmental 144 (2014) 846–854

Contents lists available at ScienceDirect

Applied Catalysis B: Environmental

journal homepage: www.elsevier.com/locate/apcatb

Effect of gold on a $NiLaO_3$ perovskite catalyst for methane steam reforming

S. Palma*, L.F. Bobadilla, A. Corrales, S. Ivanova, F. Romero-Sarria, M.A. Centeno, J.A. Odriozola

Departamento de Química Inorgánica e Instituto de Ciencia de Materiales de Sevilla, Av. Américo Vespucio, 49, 41092 Sevilla, Spain

ARTICLE INFO

Article history:
Received 21 May 2013
Received in revised form 17 July 2013
Accepted 23 July 2013
Available online 14 August 2013

Keywords:
Au–Ni catalyst
Steam reforming of methane
Carbon nanotubes
Surface alloy

ABSTRACT

The effect of gold addition to a supported Ni SRM catalyst has been studied in this work in order to determine the influence of gold on both the amount and type of carbon species formed during the reaction. The structure of the support, a mixed La–Al perovskite, determines the catalyst reducibility and Ni particle size. Gold addition affects the metal particle size increasing metal dispersion on increasing the gold content. Therefore, although gold blocks step Ni sites, the more active sites for C—H activation, and increases electron density on nickel, the higher dispersion results in an apparently higher activity upon gold addition. Moreover, gold addition increases the catalyst stability by decreasing the rate of growth of carbon nanotubes.

© 2013 Elsevier B.V. All rights reserved.

1. Introduction

Crude oil and natural gas, according to 2010 data, account for the 57% of the total energy consumed in the world and 60% of the produced hydrogen comes from natural gas [1]. Apart from the large reserves, huge amounts of natural gas are present in a wide variety of sources that can be grouped as non-conventional gas, including natural gas confined in low-permeability geological deposits, associated gas, biogas produced by anaerobic digestion of residues and product gas a result of biomass and tar gasification. Recent trends in the use of syngas are forecast the conversion in compact GTL units of inexpensive remote natural gas into liquid fuels of easier storage and transportation [2–4]. The production of hydrogen or synthesis gas from methane by partial oxidation, dry reforming and steam-reforming processes are widely studied [1]. According to the stoichiometry of the reforming reaction, steam-reforming is the most advisable process to produce hydrogen rich currents from methane. The methane steam reforming (SRM) is strongly endothermic since the high stability of the CH_4 molecule. Thus, this process requires high temperatures and the use of catalysts to achieve high methane conversion at appreciable rates [5]. The active phase of the catalysts typically used contains noble metals (Rh, Ru, Pt, Pd and Ir), cobalt, nickel or iron. High activity and resistance to the formation of carbonaceous deposits are the main advantages of noble metal containing catalysts [1], although the elevated price of these metals has led to the use of cost-effective nickel-based catalysts.

The activity of the catalysts is related to the activation of the C—H bond that is enhanced by small metallic nickel particles [5]. A successful strategy for the preparation of active SRM catalysts consists in using nanoparticles precursors with well-defined chemical structures such as perovskites, spinels, or hydrotalcites [6–8]. The reduction of these precursors results in well dispersed nickel particles on an oxide support that usually shows high catalytic activity in reforming reactions, especially combined with oxygen generators (e.g. rare earths: Ce, Pr or others), which allow controlled formation of nanoparticles, good catalytic behavior in the SRM reaction and stability of the catalyst under strong reaction conditions [9,10].

A major drawback, despite the good activity in the SRM of nickel-based catalysts, is the strong tendency of nickel to form surface coke. This may results in the total deactivation of the catalyst. Methane decomposition on the metal particle results in the formation of surface C species. The built-up of the carbonaceous layer continues until a critical concentration is reached, then carbon diffusion through the nickel particle or surface diffusion of carbon species starts driven by the carbon concentration gradient. This process results in the nucleation of carbon whiskers in the opposite side of the nickel particle. The time required to initiate the nucleation of the carbon whiskers is named induction time. The limiting step of the whole process is diffusion. Therefore, the best strategy to obtain robust catalysts is to increase the induction time to the

* Corresponding author.
E-mail address: sandra.palma@icmse.csic.es (S. Palma).

0926-3373/$ – see front matter © 2013 Elsevier B.V. All rights reserved.
http://dx.doi.org/10.1016/j.apcatb.2013.07.055

infinite (in an ideal case). As the rate for reaching the critical concentration depends on the relative rates of formation and gasification of C species, to decrease the stability of these carbon species is the usual strategy [1].

Coke gasification is favored by adding basic elements to the support. For instance, the conversion and selectivity of nickel catalysts prepared on lanthanum-modified supports are close to the thermodynamic predictions and results in minimal carbon deposits [11]. By inhibiting C-C bond formation, the resistance to coking of nickel catalysts is enhanced. Ni-alloy formation upon addition of Sn, Ge, or Ru, has been proposed as an effective method to improve the coking resistance [12]. Alloying nickel catalysts with gold also enhances nickel resistance to coking [13–15]. Carbon species are unstable in gold-alloyed nickel catalysts and can be easily removed, using a high steam-to-carbon ratio during the reaction. Gold addition to reforming catalysts also improves the reducibility of nickel by spillover effect [16] and increases the activity of nickel in the water gas shift reaction [17–19].

In a previous paper we have studied the catalytic activity in the SRM of a carefully synthesized $NiLaO_3$ perovskite supported on γ-Al_2O_3 with a controlled molecular architecture [20]. Long time experiments show the deactivated of this solid by formation of the carbonaceous species on the surface. The effect of gold addition to this SRM catalyst has been studied in this work in order to determine the influence of gold on both the amount and type of carbon species formed during the reaction.

2. Experimental

2.1. Catalyst preparation

The synthesis of the $LaNiO_3$ perovskite supported on γ-Al_2O_3 has been given elsewhere [6]. Briefly, a commercial γ-Al_2O_3 (Spheralite SCS505) was impregnated with a solution of $La(NO_3)_3{\cdot}6H_2O$ (Panreac, 99%) in distilled water and calcined at 900 °C for 4 h. This solid was further impregnated with a solution of $Ni(NO_3)_2{\cdot}6H_2O$ (Panreac, 99%) in distilled water and again treated at 900 °C during 4 h to result in a 15 at.% Ni–La (Ni/La atomic ratio equal to 1) solid. The similarities between the lattice parameters of $LaNiO_3$, $NiAlO_3$ and the (1 1 0) plane of the γ-alumina favor the formation of a perovskite monolayer on top of the alumina support [6]. This solid will be named NiLa in the following.

Gold containing catalysts were prepared by the *direct anionic exchange* (DAE) method [21]. In order to determine the influence of gold on the activity, product distribution and stability of Ni–La catalysts in the SRM, two catalysts with 0.5 and 1.0 wt.% gold loadings were synthesized. These catalysts will be referred as 0.5Au/NiLa and 1.0Au/NiLa, respectively. Adequate amounts of aqueous $HAuCl_4$ solutions are used in the exchange process to achieve the required gold loading. In a further step, the obtained solid is carefully washed with ammonia to remove surface chlorides. This process prevents the poisoning effect of chloride anions and the agglomeration of gold particles during the calcination step.

2.2. Characterization

The elemental composition of the catalysts was determined by X-ray fluorescence spectrometry (XRF) using a Panalytical AXIOS PW4400 sequential spectrophotometer with a Rh tube as source of radiation. The measurements were taken onto pressed pellets containing 6 wt.% of wax.

Powder X-ray diffraction (XRD) patterns were recorder on a Siemens D5000 diffractometer using Cu Kα radiation (40 mA, 40 kV) with 0.05° step size and 240 μs step time, over a 2θ range of 10–80°.

The textural properties were studied by N_2 adsorption–desorption isotherms at liquid nitrogen temperature. The experiments were carried out in a Micrometrics ASAP 2010 equipment. Before the analysis, the samples were outgassed for 2 h at 150 °C in vacuum.

Temperature-programmed reduction (TPR) experiments were carried out in a conventional quartz reactor connected to a TCD detector. The reactive gas stream (5% H_2 in Ar) was flowed at 50 mL/min over 50 mg of sample, and the temperature raised at 10 °C/min from room temperature to 900 °C. A molecular sieve 13X was used to retain the H_2O produced during the reduction and the CO_2 that could evolve from the surface of the solid. Quantitative analyses were done by integration of the reduction signal and comparison with hydrogen consumption of a CuO reference sample.

Scanning electron microscopy (SEM) analyses of the supports were carried out in a SEM-FEG Hitachi S4800 instrument equipped with an energy dispersive X-ray analyzer (EDX). A Zeiss ULTRA 55 high resolution FESEM equipped with in lens, secondary and backscattered electron detectors were used.

Raman spectra were recorded on a dispersive Horiva Jobin Yvon LabRaman HR800 Microscope with a 20-mW green laser (532.14 nm) without filter and using a 600 groves/mm grating. The microscope used a 50× objective with a confocal pinhole of 1000 μm. The Raman spectrometer is calibrated using a silicon wafer.

Temperature programmed oxidation (TPO) analysis were performed in a U-shaped quartz reactor under oxygen flow (21% in helium) in a temperature range of 25–900 °C at a heating rate of 10 °C/min. CO_2 evolution was monitored following the m/z = 44 signal by mass spectrometry in a Balzers Omnistar Bentchop instrument.

2.3. Catalytic reaction

The catalysts were tested using a PID Eng&Tech Microactivity set-up equipped with a 9 mm internal diameter tubular Hastelloy reactor (Autoclave Engineers). After water removal at the reactor exit, the reformate was analyzed by gas chromatography (GC) using an Agilent 6890N instrument with a Porapaq-Q column, thermal conductivity (TCD) and flame ionization detectors (FID) connected in series.

The amount of catalyst used for the experimental runs was fixed at 100 mg while the total gas flow was modified to fit the selected range of space velocities. Prior to reaction, the catalyst was reduced at 800 °C in a 100 mL/min stream of 20% H_2 in N_2 for 2 h. Before starting the experiment the reactor was N_2 flushed for at least 30 min. A constant value of 1.24 was selected in all experiments for the steam-to-carbon ratio (S/C). Methane flows of 50, 100 or 200 mL/min together with liquid water flows of 0.05, 0.1 or 0.2 mL/min were fed to the reactor to run the reaction at space velocities in the range of 67,000, 135,000 and 270,000 mL g^{-1} h^{-1} for analyzing the coking behavior of the catalysts during the SRM at 700 and 800 °C on 96 h of reaction. However, the data at the lowest space velocity were discarded since the methane conversion was too high for obtaining reliable results for the deactivation process. The dry gas was analyzed by GC every 15 min.

Methane conversion (X_{CH_4}) was calculated according to Eq. (1).

$$X_{CH_4} = \frac{[CH_4^{in}] - [CH_4^{out}]}{[CH_4^{in}]} \times 100 \quad (1)$$

where $[CH_4^{in}]$ and $[CH_4^{out}]$ indicate the concentration of methane at the inlet and outlet of the reactor respectively.

Table 1
Chemical composition, surface area ($m^2\ g^{-1}$), pore volume (V_p, $cm^3\ g^{-1}$) and average pore diameter (D, nm) of the prepared catalysts.

Composition (wt.%)					Composition (at.%)		Textural properties			Ni/La
Catalysts	Al_2O_3	NiO	La_2O_3	Au	La	Ni	S_{BET}	V_p	D	
NiLa	73.3	8.8	17.9	–	6.6	7.2	36	0.28	18	1.04
0.5Au/NiLa	73.5	8.2	17.7	0.55	6.6	6.7	34	0.38	20	0.98
1.0Au/NiLa	77.2	6.2	15.6	0.94	5.7	5.0	36	0.32	19	0.84

3. Results and discussion

Table 1 shows the chemical composition and textural properties of the prepared catalysts. The gold-modified nickel catalysts retain the textural properties of the parent catalyst.

The gold content of the prepared catalysts is close to the target values; however, the nickel content of the gold-doped catalysts is slightly lower than that of the bare nickel catalyst. The partial elimination of supported transition metals usually occurs as a consequence of the ammonia-washing step included in the gold catalyst preparation route, soluble ammonia complexes of nickel are formed accounting for the Ni concentration observed upon gold addition [21].

Synthesis of perovskite precursors is generally performed in order to obtain, after reduction, homogeneous well dispersed nickel nanoparticles. In addition, it has been suggested that the strong interaction between nickel and lanthanum in the perovskite structure prevents nickel from sintering [22,23]. Moreover, the size of the crystallites formed during reduction depends on the structure and texture of the perovskite [24]. The synthesis of the Ni catalyst precursor implies two calcination steps at 900 °C. In the first calcination step a surface $LaAlO_3$ perovskite phase is formed [6]. After nickel impregnation and further calcination at 900 °C either a $NiLaO_3$ perovskite on top of the La–Al perovskite [6] or the $LaNi_{1-x}Al_xO_3$ mixed oxide phase [25] may be formed. The XRD pattern of the nickel catalyst precursor shows the presence of a cubic perovskite phase together with diffraction lines of the γ-Al_2O_3 phase. Both $NiLaO_3$ and $LaAlO_3$ perovskite crystallizes in the orthorhombic space group $R\bar{3}c$, the lattice parameters of these phases differ by less than 2% resulting in hardly distinguishable XRD patterns since most of their diffraction lines overlaps (Fig. 1A) [26,27]. Although the similar structure and lattice parameters of both perovskite prevents a clear distinction between them, their presence may be hypothesized since diffraction lines corresponding to NiO are absent upon calcination at 900 °C. Upon H_2-reduction at 800 °C (Fig. 1B), the XRD patterns show diffraction lines corresponding to γ-Al_2O_3, an orthorhombic perovskite phase and metallic nickel evidenced by diffraction lines at 2θ angles of 44.3°, 51.60° and 76.08° corresponding to the (1 1 1), (2 0 0) and (2 2 0) planes, respectively. The formation of metallic nickel and the absence of diffraction lines corresponding to the spinels $NiLa_2O_4$ or $NiAl_2O_4$ allows suggest that the nickel perovskite is either reduced to metallic nickel or remains partially stabilized on top of the LaAl perovskite phase.

Metallic Au nanoparticles in the case of the gold-containing samples are not observed by XRD, pointing either to the presence of very small well-dispersed gold nanoparticles or to the formation of a Ni–Au solid solution after the reduction treatment. The estimation of the cubic lattice parameter for the Ni phase from the XRD patterns (a = 0.352 nm) appears to be irrespective of the presence or absence of gold in the catalysts, suggesting the formation of the very small gold nanoparticles on the support surface. Although FCC metals like nickel and gold are not miscible at room temperature, according to Hume-Rothery rules, it has been proposed that gold forms stable surface alloy in the first atomic layer of nickel [28,29]. Usually, at T > 300 °C the molar fractions of gold of the prepared catalysts are outside the spinodal curve allowing metastable Au–Ni solid solutions [30]. Monte Carlo simulations have shown that gold atoms are exclusively located at the Ni particle, preferentially sitting on nickel edge and ink sites of low-index planes. This results in an average coordination number around Au of five Ni atoms [31]. Nevertheless, Chin et al. [11] observed that on increasing the Au content from 0.2 wt.% to 1 wt.% the Au–Ni average coordination number decreases while the Au–Au average coordination number increases.

The nickel crystallite size estimated through the Scherrer's equation is 16 nm, and remains hardly altered for the 0.5Au/NiLa catalyst and decreases up to 7 nm for the 1.0Au/NiLa one, pointing to some kind of interaction between nickel and gold. Considering the all explained above, it can be assumed that upon reduction at high temperature the Au–Ni metastable solid solution is formed which on cooling undergoes a spinodal decomposition resulting in a well-dispersed gold phase on Ni FCC crystals. Therefore, the Au–Ni catalysts may be described as gold atoms placed on under-coordinated step sites of nickel crystallites that sit on a La-containing perovskite phase supported on γ-Al_2O_3. This model agrees well with the theoretical calculations of Bengaard and

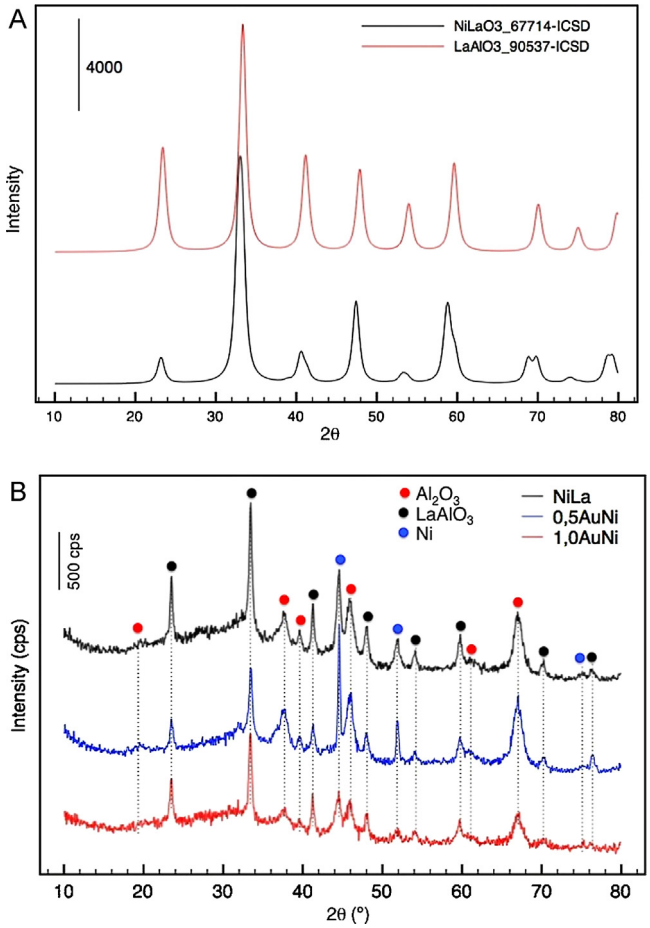

Fig. 1. (A) XRD patterns of the reduced samples; (B) simulated XRD patterns of $NiLaO_3$ and $LaAlO_3$.

Table 2
Average crystallite size of nickel (D_{Ni}), reduction degree (RD), surface area of metallic nickel (S_{met}) and total number of surface nickel sites (N_s) of the reduced catalysts.

Catalysts	D_{Ni} (nm)	RD (%)	S_{met} ($m^2\ g_{cat}^{-1}$)	N_s (10^{19} at g_{cat}^{-1})	100Au/N_s
NiLa	15	48	1.8	3.2	0
0.5Au/NiLa	17	52	1.8	3.2	52
1.0Au/NiLa	7	72	4.6	8.3	34

co-workers [14]. Regarding the structural models, simulation of the Ni–Au particles assumed truncated octahedron geometry for the Ni particles consisting of 583 Ni atoms and 100 Au atoms deposited preferentially on the step sites [31]. Using this geometry, the planar density calculation for the (1 1 1) and (1 0 0) FCC index planes and the particle size of Ni deduced from the XRD measurements allowed us to make rough estimation of the number of surface gold atoms for the corresponding Ni particle size as presented in Table 2. This geometry results in a 1:1 and 2:1 Ni:Au surface ratios for the 0.5Au/NiLa and 1.0Au/NiLa catalysts, respectively. This ratio is well above the number of low coordinated nickel sites on the nickel surface for the 0.5Au/NiLa catalyst but closely matches the number of the step sites for the 1.0Au/NiLa catalyst when the truncated octahedron shape is assumed. Both experiments and DFT calculations on the Au/Ni systems have shown that above 0.4 monolayers of Au surface spinodal decomposition takes place and the Au–Ni surface alloy undergoes a phase transition that results in the nucleation of gold clusters on the Ni surface [32–34]. If we assume the existence of a surface alloy, whatever the gold loading, the coverage once considered the particle size, is below 0.4 monolayers, which should result in the formation of gold clusters on nickel as the gold loading increases from a certain value. This is actually the case of the 0.5Au/NiLa catalyst but not for the 1.0Au/NiLa for which an exact match of the number of the step sites was found.

Despite of the effect of gold addition on the atomic organization an influence on the reduction behavior is also expected. However, the TPR profiles of the prepared catalysts remain unaltered whatever the gold content (Fig. 2). The catalyst reduction occurs in a single step with a maximum in the reaction rate at ca. 860 °C. This maximum shows a minute shift toward lower temperatures on increasing the gold content. The observed reduction temperature is higher than the one usually reported for this type of solids. $NiLaO_3$ perovskite is completely reduced at around 750 °C, although lower reduction temperatures are attained mostly depending on the oxygen-defect structure of the prepared perovskite [35,36]. Most of literature data agrees in a partial reduction of Ni^{3+} to Ni^{2+} at low temperatures (300–450 °C) resulting in $La_2Ni_2O_5$ or $La_4Ni_3O_{10}$ phases that are the result of oxygen vacancies generated shear planes during the reduction process [37]. Further decomposition

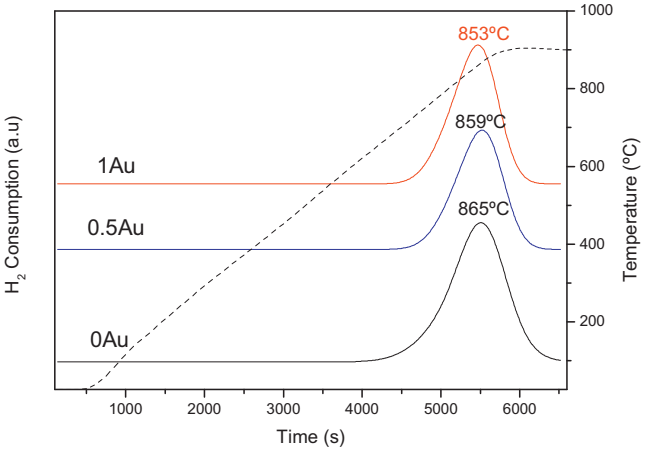

Fig. 2. H_2-TPR profiles of the prepared catalysts.

of these new phases at high temperatures (500–700 °C) results in either metallic nickel or to a new spinel intermediate, La_2NiO_4, further reduces to Ni^0 [36,38]. Whatever the reduction mechanism, it results in a complex TPR pattern showing 2 or 3 maxima and complete reduction at temperatures below 750 °C. However, higher reduction temperatures are observed, up to 900 °C, on decreasing the nickel content of the $LaNiO_3$ perovskite [39].

Slagtern et al. [25] studied the effect of the formation of solid solutions in the reducibility of the $LaNiO_3$–$LaAlO_3$ system. They found for these $LaNi_{1-x}Al_xO_{3-d}$ solid solution phases for which a complete reduction of nickel occurs at temperatures as high as 980 °C, being higher as the nickel content decreases. As the Ni-to-La ratio is close to the unity, Table 1, low nickel contents cannot be invoked for explaining the high reduction temperature, remaining the formation of a complete miscible $LaNiO_3$–$LaAlO_3$ solid solution with low nickel content the more feasible explanation for the high temperature observed in the TPR profiles (Fig. 2). ABO_3 perovskites may be envisaged as an ordered stack of BO_2-AO-BO_2 layers with the small B cation at the center of a framework of corner-sharing oxygen octahedra. The perovskite tendency toward anion deficiency is determined by the properties of the transition metal cation, ranging from negligibly small δ values in $ABO_{3-\delta}$ as in $LaAlO_3$, to a remarkably high concentration of the anion vacancies as in $LaNiO_3$ [37]. The formation of shear planes requires defects grouped along characteristic directions in the crystal, typically [1 0 0] rows, which transforms the BO_6 octahedra into planar BO_4 polyhedra. The nature of B determines the ordering of the oxygen vacancies. If the B cation is hardly reducible, oxygen vacancies occurs at very high temperatures, as in aluminum. On the contrary, cations that tend to form square planar polyhedra lose oxygen and form intermediate phases at low temperatures. Therefore, the morphological constrain induced by the γ-alumina support on the perovskite layer and the random distribution of Ni and Al at the B sites of the perovskite prevents oxygen vacancies to group, allowing the occurrence of nickel reduction only at high temperatures. Moreover, the absence of a peak at 350 °C corroborates that amorphous NiO is not present in the samples, which is in accordance with XRD data.

The catalyst reducibility has been estimated from the area under the TPR curve assuming the global process

$$2LaNiO_3 + 3H_2 \overset{860\,^\circ C}{\longrightarrow} La_2O_3 + 2Ni^0 + 3H_2O \quad (2)$$

as the only one contributing to H_2 consumption. On increasing the amount on gold, the percentage of reduced nickel increases from the 48% of the bare nickel catalyst up to 52 and 72% for the catalysts containing 0.5 and 1.0 wt.% Au, respectively, Table 2.

The increasing of the degree of reducibility when gold is present in the solid may be explained by spillover effect [25], and implies that the amount of metallic nickel on the surface is higher for the solid containing 1 wt.% Au, despite the lower amount of nickel in the final catalyst.

In all cases, hydrogen consumption was lower than expected, suggesting, that at least, a part of the nickel is not being reduced, probably due to the strong interaction with the La in the perovskite structure and its reduced mobility of it. This fact does not contradict the XRD results, because, as explained before, the most intense $LaNiO_3$ and $LaAlO_3$ diffraction peaks are hardly differentiated.

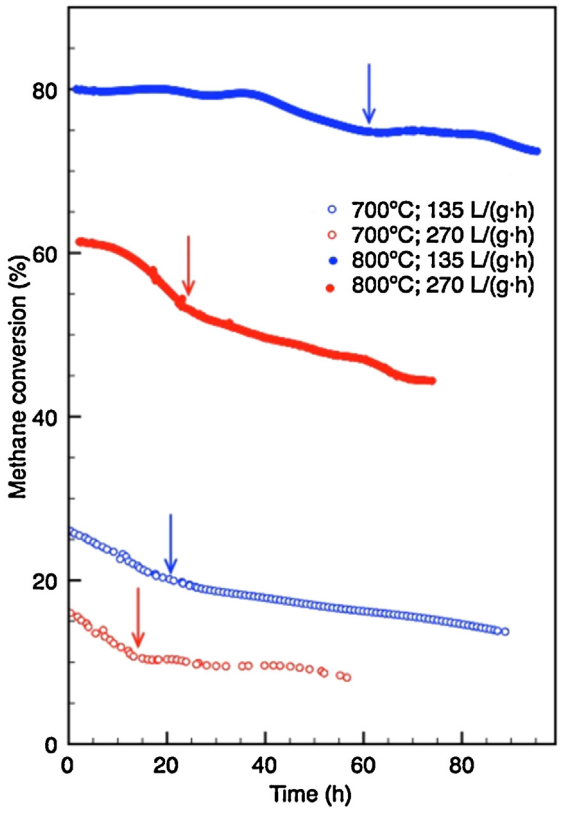

Fig. 3. Evolution of the methane conversion with time on stream of NiLa catalyst in the SRM as a function of reaction temperature and space velocity.

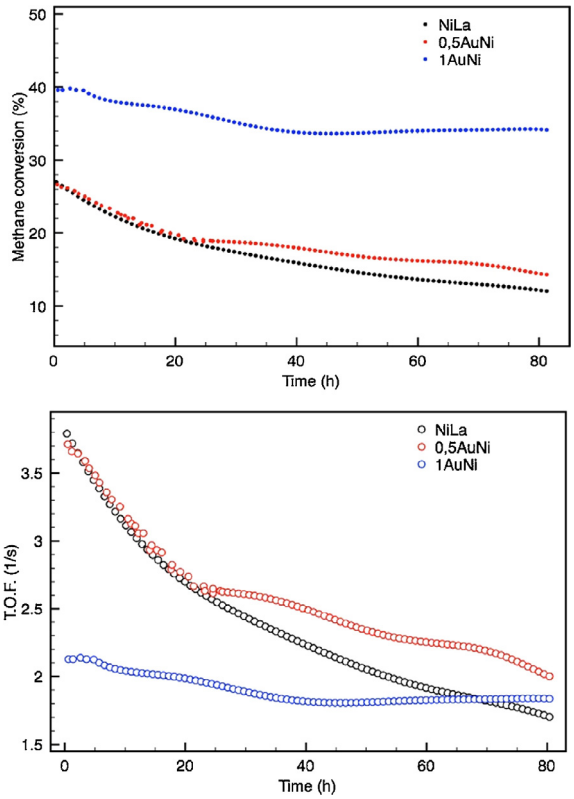

Fig. 4. (A and B) Methane conversion for the catalysts containing gold compared with the NiLa sample.

3.1. Catalytic activity

The simplest way of describing SRM is considering the methane dissociation producing adsorbed carbon and gaseous hydrogen and further gasification of the adsorbed carbon by water for producing carbon oxides and hydrogen. Carbon species are formed on the catalyst surface upon interaction with methane. Once surface carbon reaches a certain amount, the critical concentration, diffusion starts, with the driving force being the concentration gradient. This critical concentration is attained at a rate that depends on the relative rates of carbon formation through methane dissociation and carbon gasification [1]. The time needed for attaining of the critical concentration is then the induction time. It is well known, that the operation conditions determine the formation and gasification rates, as well as the induction times. Fig. 3 presents the influence of temperature and space velocity on the activity of the Ni–La catalyst in the SRM reaction. For this catalyst, longer induction times are observed at high temperatures and low space velocities, the more advisable situation from a practical point of view. Methane conversion decreases smoothly with time, whatever the conditions tested in the SRM. However, after an induction time, carbon grows at a constant rate [1] and therefore methane conversion from that point forth, decreases linearly. This is observed experimentally by the change of the slope in the activity curves (indicated by arrows in Fig. 3). The induction period ends later at higher reaction temperatures and lower space velocities, which correlated to the carbon formation model should mean longer times to a carbon-saturated nickel surface.

For studying the effect of gold addition on the coking of Ni–La catalysts, operation conditions that minimize the induction time should be selected. Therefore, the best temperature–space velocity combination for obtaining low induction times and enough C—H bond activation upon gold addition are placed in the low side of the studied range: 700 °C and 135,000 mL g^{-1} h^{-1}.

The methane conversions for the catalysts containing gold is compared to NiLa in the selected conditions and shown in Fig. 4. On adding 0.5 wt.% gold to the NiLa catalyst, the initial methane conversion (~25%) is hardly modified, but after the induction time (~20 h) methane conversion is slightly higher and the deactivation rate seems to be slower for the Au-containing catalyst (Fig. 4A). With the increase of the gold loading to 1 wt.%, the initial methane conversion increases up to 45%, and after an initial loss of activity, the conversion stabilizes at ca. 35%. The induction time is shorter and the stability higher than for NiLa and 0.5 wt.% gold catalyst. Apparently, gold addition increases the activity of the nickel catalyst since methane conversion is higher for lower amount of nickel (Table 1). Taking into consideration the nickel particle size, the selected shape of the Ni particles (truncated octahedron) that results in ca. 75% of (1 1 1) faces and 25% of (1 0 0) nickel faces the number of Ni surface atoms can be calculated (Table 2). Then the activity could be normalized to the available Ni surface atoms (TOF number) as presented in Fig. 4B. Similar TOF numbers for the NiLa and 0.5Au/NiLa catalysts and decrease of the activity per surface nickel sites in the case of the 1.0Au/NiLa catalyst was observed. Again, referring to the geometrical approach and the Ni particle size, for the 1.0Au/NiLa catalyst, where the Au coverage closely matches the number of the Ni step sites the decrease of the TOF number could be related to the diminishing of the number of available Ni step sites responsible for the C—H bond activation. The same was reported by the Rostrup-Nielsen and Alstrup [40], using density functional theory (DFT) calculations, who predicts that gold neighbors increase the activation barrier for the methane dissociation, on nickel and, hence, that Au inhibits methane dissociation e.g. the first C—H bond activation. However, as the particle size is much bigger for the 0.5Au/NiLa catalyst the surface coverage of gold largely

exceed 0.4 monolayers in this solid, favoring the formation of gold clusters and liberating nickel step sites. The later allows explaining the similar TOF numbers for the NiLa and 0.5Au/NiLa catalysts.

All the observed trends may be understood not only considering the effect of gold on the activation of the C—H bond by nickel, but in the same time on the oxidation rate of the carbonaceous deposits. As indicated above, the adsorption of methane preferentially proceeds on step sites resulting in adsorbed C species that further react with adsorbed oxygenated groups coming from water adsorption to give H_2 and CO [1]. However, these C species on nickel step sites are stable and its reaction/gasification is difficult. If these adsorbed carbon species disappear at low rate, the concentration of C species on the metallic surface after a certain time is high enough to initiate diffusion in the metallic particle and the growth of carbon nanotubes. Then the evolution of the catalytic activity as a function of time on stream must be associated to the formation of carbon. At a steady state, a certain quantity of methane is consumed in the growing step. As the limiting step is the initial diffusion in the metallic particles, it may occur that the concentration of carbonaceous species on the surface becomes high enough to cause the total deactivation of the solid.

According to the TPR data, gold addition improves the catalyst reducibility (Table 2) and therefore, a higher number of active sites and higher conversion are expected, promoted by the increase of the gold content. As carbon nanotubes formation is initiated at the step sites where gold is preferentially bound, higher gold content implies a lower number of sites for carbon formation. Since the electronic density of gold is more extended than that of nickel, the Au–Ni interaction results in a modification of the oxidation states of Ni (electron density richer) and Au (electron density poorer) [13–15]. The Ni atoms in the coordination sphere of gold atoms acquire a higher electronic density so decreasing the "effective" coordination number and consequently decreasing the energy of the surface [13]. This means that gold addition decreases the activity of the surrounding nickel atoms and at the same time, the stability of the adsorbed carbon species decreases and a higher rate of gasification) is expected resulting in longer induction time.

Carbon gasification results in the formation of carbon oxides and hydrogen according to the following reactions:

$$C + H_2O \rightarrow CO + H_2 \quad (3)$$

$$CO + H_2O \rightarrow CO_2 + H_2 \quad (4)$$

These reactions require the adsorption/activation of water molecules. Water interacts weakly with the (1 1 1) metal surfaces, the binding energy, or the order of the hydrogen bond, on Ni(1 1 1) being higher than on Au(1 1 1), according to DFT calculations [41]. Water mostly adsorb on (1 1 1) faces in molecular form, since water dissociation into H and OH present a relatively high energy barrier, 0.89 eV on Ni(1 1 1) surfaces, and a further barrier of 0.97 eV need to be overcome to dissociate OH into O and H on this surface [42]. Experimentally, however, only on Ni stepped surfaces water dissociation has been observed [43]. The binding energy of OH relative to OH(g) increases as the oxophilicity increases, therefore it is higher for Ni than for Au [25]. The Au–Ni interaction affects the gasification rate since gold atoms sits on Ni step sites diminishing the number of surface sites able of dissociating water and hence the gasification rate should decrease, as experimentally observed, for AuNi/YSZ catalysts [44]. However, this Ni–Au interaction decreases the electron density on gold atoms [11] making them more oxophilic and favoring water dissociation on gold sites and hence increasing the oxidation rate of CO by hydroxyl groups. The decrease in the gasification rate upon gold addition is relatively less important than the activity decrease for methane dissociation, since the later preferentially occurs at step sites that are covered by gold while water dissociation occurs preferentially at terraces [45].

Table 3
Product distribution for all catalysts studied in the SRM reaction carried out at 700 °C and 135,000 mL g^{-1} h^{-1}.

Catalyst	CH_4 conversion[a] (%)	CO/CO_2	H_2/CO
Ni–La	14	2.0	5.3
0.5Au/Ni–La	16	2.0	5.3
1.0Au/Ni–La	34	1.3	7.1

[a] After conversion stabilization.

The influence of gold on the oxidation of the carbonaceous species is reflected in the product distribution, Table 3. For every catalyst, the relative amounts of H_2, CO and CO_2 remains almost unaltered with time on stream. However, while the addition of 0.5 wt.% Au hardly affects the product distribution with respect to the parent Ni catalyst, which suggest that gold effect just consists in partially blocking Ni active sites, increasing the gold amount to 1 wt.%, the relative amounts of H_2 and CO_2 increases, suggesting that Au, in this case, favors the water–gas-shift reaction. The reactivity in the WGS (Eq. (4)) depends on the relative stability of the hydroxyl group that is favored on electron deficient metals. In the Au–Ni catalysts, isolated gold atoms are electron deficient if isolated in the Ni matrix [11,13,15], as in the case of 1.0Au/NiLa. On the contrary, as for the 0.5Au/NiLa where the gold coverage exceeds 0.4 monolayers, the Ni–Au alloy phase transforms in Au clusters [32–34] deposited on the Ni surface and charge transfer from gold to nickel no longer exists [11] and WGS reaction is disfavored.

3.2. Characterization of catalyst after reaction

SEM micrographs of the catalysts after 96 h of reaction are shown in Fig. 5. In every case, carbon nanotubes are observed in the micrographs as filaments. Qualitatively from these figures, it appears that the global amount of carbon nanotubes decreases as the gold content increases. This is related to the decrease of the number of sites on which the nanotubes are initiated and with the higher instability of the carbonaceous species induced by the presence of gold. A deep characterization of the carbon nanotubes formed was carried out by TEM, Raman spectroscopy and TPO analysis.

The formation of carbon nanotubes was verified by TEM. Fig. 6 shows images of the Ni–La catalyst after reaction. As previously reported for $NiLaO_3$ precursor, multi-wall carbon nanotubes (MWCNT) are formed. The inner diameter has a range of 8–12 nm, and the outer one of 20–35 nm. Even thought that the growth of this type of nanotubes is favored on the $NiLaO_3$ precursor, they have been previously reported for NiO, $NiLa_2O_3$ and $Ni/CuO/Al_2O_3$ catalysts [24].

The existence of carbon nanotubes in the spent catalysts is clearly observed by Raman (Fig. 7). In every case, two main bands associated to carbon nanotube structures dominate the Raman spectra. The band, at 1350 cm^{-1} (D band) contains information on the disturbances in the sp^2 hybridization of carbon atoms and on the degree of disorder within the carbon nanotube. The first overtone of this band is also observed at 2680 cm^{-1}. The band around 1580 cm^{-1} (G band) is due to the tangential stretching of carbon atoms in a two-dimensional hexagonal lattice. In some cases, two bands may be differentiated in this region, the called G^+ band, due to atomic displacements along the axis of the carbon nanotube (~1587 cm^{-1}) and the G^- band associated to vibrations perpendicular to the axis (~1550 cm^{-1}). The Raman shift of the G^- band decreases on decreasing the particle diameter, while the one of the G^+ is practically independent of the particle diameter. Therefore, the difference between these two bands may be used to estimate the particle size. The higher is the difference the smaller the

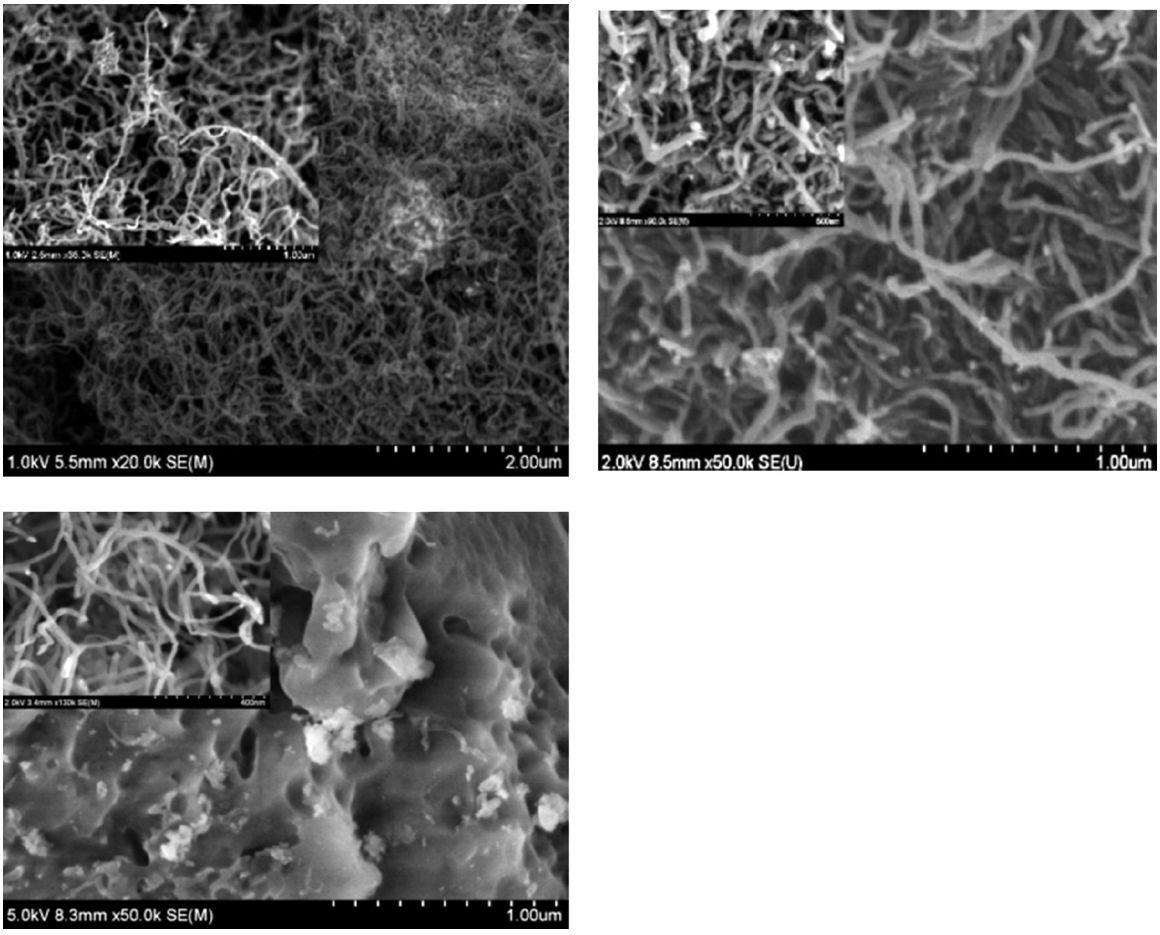

Fig. 5. 500 nm and 1 μm pictures of NiLa catalyst (A), 0.5 wt.% AuNi catalyst (B), and 1 wt.% AuNi catalyst (C), after 96 h on SRM stream. T = 700 °C and GHSV = 135,000 mL g^{-1} h^{-1}.

particle diameter. In the Raman spectra of the spent catalysts only one band is detected in this region, which is related to the observation of multiwall nanotubes (MWCNT). As observed by TEM there are a relatively wide distribution of diameter sizes, which results in broad Raman lines; therefore, as the splitting of the G^+ and G^- bands in MWCNT is very small, this splitting is hardly differentiated in our case. Moreover, the value of the intensity ratio between the G and D bands, I_G/I_D, is usually used to estimate the content of defects in the carbon nanotubes. For instance, arc discharge methods allow synthesizing highly structured carbon nanotubes with a very low concentration of defects. For these highly structured CNT, the reported values of the I_G-to-I_D ratio is in the range of 20–50. In our case, the I_G-to-I_D ratios are 0.96, 0.59 and 0.58 for the catalysts containing 0, 0.5 and 1 wt.% Au. These values indicate that the differences induced by gold in the CNT crystallinity are quite small, but by a slightly increase in the number of defects within the CNT upon gold addition. The presence of defects in carbon nanotubes is related to the growth rate of the nanotubes; the higher is the number of defects the faster the growth rate. These data are in accordance with our previous considerations, therefore, on adding gold to the nickel catalyst not only the induction time is modified by the presence of gold, but the CNT growth rate is also reduced.

Temperature programmed oxidation of the spent catalysts (TPO) allows completing the structural picture of the surface carbon species deduced by Raman spectroscopy. This technique provides information on the amount and nature of the coke formed on the catalyst. The area under the evolved CO_2 (m/z = 44) curve as a function of time, during the TPO experiments, evaluates the amount of carbon formed on the spent catalyst (Fig. 8). Moreover, the type of carbonaceous species present on the catalyst surface determines the temperature at which the carbon oxidation rate reaches a maximum. The maximum rate for CO_2 evolution is in the range of 630–700 °C depending on the amount of gold. Thus, as higher the amount of gold the lower the temperature of the peak maximum in the TPO profiles. Moreover, the total amount of CO_2 produced is inversely proportional to gold loading as expected considering that gold blocks nickel step sites, which are the sites showing the highest specific activity in the C—H bond activation. From a qualitative point of view, the shift of the TPO peak to lower temperatures on increasing the gold content agrees well with the presence of defects within the CNT induced by gold addition, as detected by Raman, and with the increase in the carbon gasification rate upon gold addition.

From a quantitative point of view, a decreasing of the area of TPO peak area decreases on increasing the gold content of the catalysts, Table 4. These values clearly indicate a diminution of the amount

Table 4
Normalized mass relative area of TPO profiles of the spent catalysts after 96 h in stream at 700 °C and 135,000 mL g^{-1} h^{-1}.

Catalysts	Relative area
NiLa	13.60
0.5AuNi	8.60
1.0AuNi	6.45

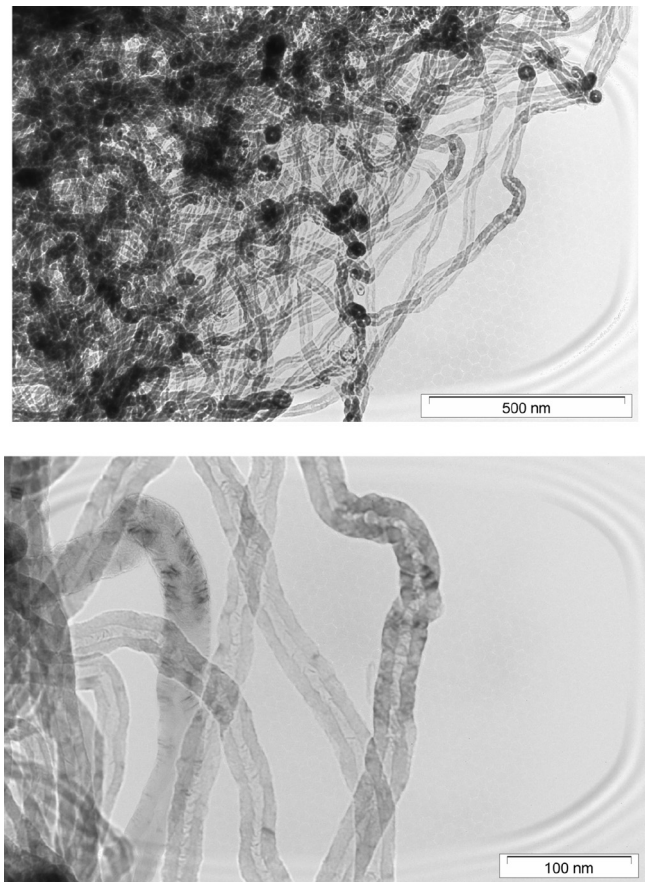

Fig. 6. TEM pictures of NiLa spent catalyst. 96 h of reaction at 700 °C and 135.000 mL g^{-1} h^{-1}.

of carbonaceous species formed on adding gold to the Ni catalyst, keeping constant the reaction time and operational variables. The rate of formation of carbon nanotubes must be proportional to the number of surface sites able to initiate the C—H bond activation that is the number of step sites. Since the gold is preferably located in these sites, the direct consequence is at least the partial inhibition of the cooking process.

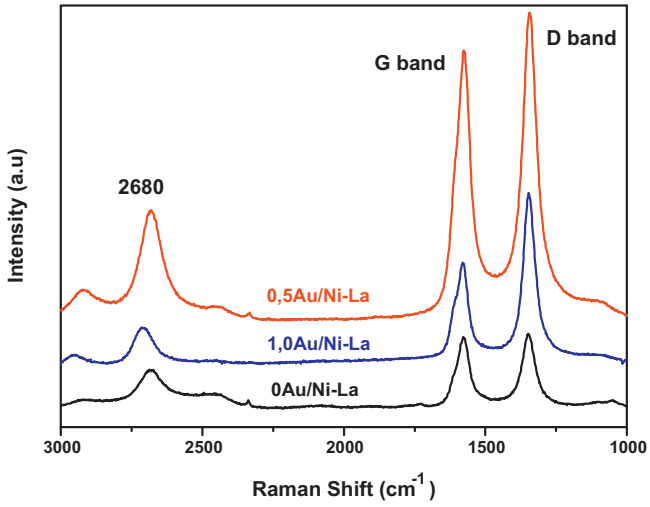

Fig. 7. Raman spectra of the spent catalysts after 96 h on stream.

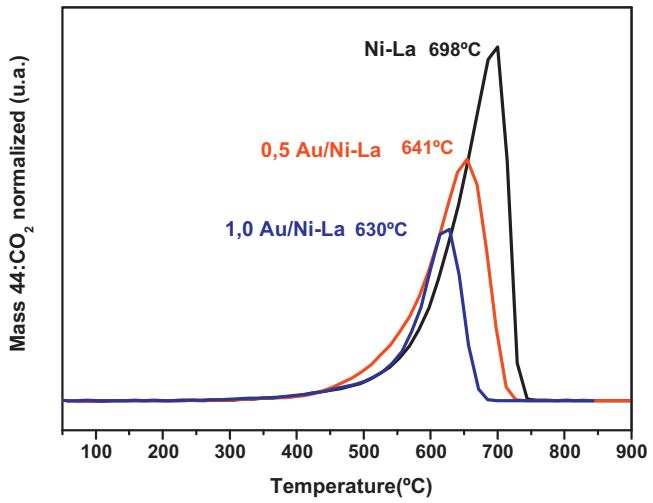

Fig. 8. TPO profiles of the spent catalysts after 96 h on the reaction stream at 700 °C and 135,000 mL g^{-1} h^{-1}.

4. Conclusions

The effect of gold addition to a supported Ni SRM catalyst prepared by nickel impregnation and further calcination at 900 °C on a $LaAlO_3/Al_2O_3$ surface has been studied. XRD patterns do not allow distinguishing if either a $NiLaO_3$ perovskite on top of the La–Al perovskite or the formation of a $LaNi_{1-x}Al_xO_3$ mixed oxide phase constitute the precursor phase of the nickel catalyst. However, TPR data strongly suggest the formation of the later phase with random occupancy of Ni and Al at the B sites. Reduction of this phase occurs only at high temperature in a single step, with the effect of gold consisting in slight decrease of the reduction temperature and considerable increase of the reduction degree. In the same time, the perovskite structure prevents nickel sintering and explains the small size of the nickel particles ranging 17–7 nm, the smaller size corresponding to the higher Au loading, for which the formation of a surface Ni–Au alloy may be the responsible for the smaller particle size.

The increasing of the degree of reducibility when gold is present, together with the smaller particle size, implies that the amount of metallic nickel on the surface (which is the active phase in the steam reforming reaction) is higher for the solid containing 1 wt.% Au, despite the lower amount of nickel in the final catalyst. This results in an apparently higher methane conversion for the 1.0Au/NiLa catalyst compared to the parent Ni catalyst. However, when expressed in TOF number, an increase of the gold content reveals lowering of the activity of the surrounding nickel atoms. And at the same time, the gold addition results in the decreases of the stability of the adsorbed carbon species and a higher rate of gasification, resulting in longer induction time for catalyst deactivation.

Acknowledgements

Financial support for this work has been obtained from the Spanish Ministerio de Ciencia e Innovación (ENE2009-14522-C05-01) co-funded by FEDER funds from the European Union. L. Bobadilla thanks the "Junta de Andalucia" for his fellowship with the project POG-TEP01965. S. Palma thanks to the same Ministery for her fellowships (ENE2009-14522-C05-01). S. Ivanova acknowledges MEC for her contract Ramon y Cajal.

References

[1] J.R. Rostrup-Nielsen, L.J. Christensen, Concepts in Syngas Manufacture, Imperial College Press, London, 2011.

[2] G. Arzamendi, P.M. Diéguez, M. Montes, J.A. Odriozola, E. Falabella Sousa-Aguiar, L.M. Gandía, Chem. Eng. J. 160 (2010) 915–922.
[3] A.Y. Tonkovich, B. Yang, S.T. Perry, S.P. Fitzgerald, Y. Wang, Catal. Today 120 (2007) 21–29.
[4] G. Kolb, T. Baier, J. Schurer, D. Tiemann, A. Ziogas, H. Ehwald, P. Alphonse, Chem. Eng. J. 137 (2008) 653–663.
[5] A. Yamaguchi, E. Iglesia, J. Catal. 274 (2010) 52–63.
[6] M.J. Capitán, M.A. Centeno, P. Malet, I. Carrizosa, J.A. Odriozola, A. Márquez, J. Fernández Sanz, J. Phys. Chem. 99 (1995) 4655–4660.
[7] V.A. Tsipouriari, X.E. Verykios, J. Catal. 179 (1998) 292–299.
[8] M. Muñoz, S. Moreno, R. Molina, Int. J. Hydrogen Energy 37 (2012) 18827–18842.
[9] C.E. Daza, J. Gallego, F. Mondragón, S. Moreno, R. Molina, Fuel 89 (2010) 592–603.
[10] O. Gamba, S. Moreno, R. Molina, Int. J. Hydrogen Energy 36 (2011) 1540–1550.
[11] Y.-H. Chin, D.L. King, H.-S. Roh, Y. Wang, S.M. Heald, J. Catal. 244 (2006) 153–162.
[12] D.L. Trimm, Catal. Today 49 (1999) 3–10.
[13] F. Besenbacher, I. Chorkendorff, B.S. Clausen, B. Hammer, A.M. Molenbroek, J.K. Nørskov, I. Stensgaard, Science 279 (1998) 1913–1915.
[14] H.S. Bengaard, J.K. Nørskov, J. Sehested, B.S. Clausen, L.P. Nielsen, A.M. Molenbroek, J.R. Rostrup-Nielsen, J. Catal. 209 (2002) 365–384.
[15] P. Kratzer, B. Hammer, J.K. Norskov, J. Chem. Phys. 105 (1996) 5595–5605.
[16] K. Yoshida, N. Begum, S. Ito, K. Tomishige, Appl. Catal. A 358 (2009) 186–192.
[17] T. Tabakova, V. Idakiev, D. Andreeva, I. Mitov, Appl. Catal. A 202 (2000) 91–97.
[18] T. Tabakova, F. Boccuzzi, M. Manzoli, J.W. Sobczak, V. Idakiev, D. Andreeva, Appl. Catal. B 49 (2004) 73–81.
[19] T. Ramírez-Reina, W. Xu, S. Ivanova, M.A. Centeno, J. Hanson, J.A. Rodriguez, J.A. Odriozola, Catal. Today 205, 2013, 41-48.
[20] D. Hufschmidt, L.F. Bobadilla, F. Romero-Sarria, M.A. Centeno, J.A. Odriozola, M. Montes, E. Falabella, Catal. Today 149 (2010) 394–400.
[21] S. Ivanova, C. Petit, V. Pitchon, Appl. Catal. A 267 (2004) 191–201.
[22] S. Takenaka, Y. Shigeta, E. Tanabe, K. Otsuka, J. Phys. Chem. B 108 (2004) 7656.
[23] T. Maneerung, K. Hidajat, S. Kawi, Catal. Today 171 (2011) 24–35.
[24] M. Kuras, Y. Zimmermann, C. Petit, Catal. Today 138 (2008) 55–61.
[25] A. Slagtern, U. Olsbye, R. Blom, I.M. Dahl, H. Fjellvag, Appl. Catal. A 145 (1996) 375–388.
[26] C.J. Howard, B.J. Kennedy, B.C. Chakoumakos, J. Phys.: Condens. Matter 12 (2000) 349–365.
[27] J.L. Garcia-Munoz, J. Rodriguez-Carvajal, P. Lacorre, J.B. Torrance, Phys. Rev. B 46 (1992) 4414–4425.
[28] L.P. Nielsen, F. Besenbacher, I. Stensgaard, E. Lægsgaard, C. Engdahl, P. Stoltze, K.W. Jacobsen, J.K. Norskov, Phys. Rev. Lett. 71 (1993) 754–757.
[29] D.O. Boerma, G. Dorenbos, G.H. Wheatley, T.M. Buck, Surf. Sci. 307–309 (1994) 674–679.
[30] J. Wang, X.G. Lu, B. Sundman, X. Su, CALPHAD 29 (2005) 263–268.
[31] A.M. Molenbroek, J.K. Nørskov, B.S. Clausen, J. Phys. Chem. B 105 (2001) 5450–5458.
[32] W. Fan, X.G. Gong, Surf. Sci. 562 (2004) 219–225.
[33] L.P. Nielsen, F. Besenbacher, I. Stensgaard, E. Laegsgaard, C. Engdahl, P. Stoltze, J.K. Norskov, Phys. Rev. Lett. 74 (1995) 1159–1162.
[34] F. Besenbacher, J.V. Lauritsen, T.R. Linderoth, E. Laegsgaard, R.T. Vang, S. Wendt, Surf. Sci. 603 (2009) 1315–1327.
[35] J.L.G. Fierro, J.M.D. Tascon, L. Gonzalez Tejuca, J. Catal. 93 (1985) 83–87.
[36] C. Batiot-Dupeyrat, G. Valderrama, A. Meneses, F. Martinez, J. Barrault, J.M. Tatibouet, Appl. Catal. A 248 (2003) 143–151.
[37] A.M. Abakumov, J. Hadermann, G. van Tendeloo, E. Antipov, J. Am. Ceram. Soc. 91 (2008) 1807–1813.
[38] G. Sierra Gallego, C. Batiot-Dupeyrat, J. Barrault, E. Florez, F. Mondragon, Appl. Catal. A 34 (2008) 251–258.
[39] H. Provendier, C. Petit, A. Kiennemann, Stud. Surf. Sci. Catal. 130 (2000) 683.
[40] J.R. Rostrup-Nielsen, I. Alstrup, Catal. Today 53 (1999) 311–316.
[41] A.A. Phatak, W.N. Delgass, F.H. Ribeiro, W.F. Schneider, J. Phys. Chem. C 113 (2009) 7269–7276.
[42] M. Pozzo, G. Carlini, R. Rosei, D. Alfe, J. Chem. Phys. 126 (2007) 164706.
[43] C. Mundt, C. Benndorf, Surf. Sci. 287 (1993) 119–124.
[44] N.C. Triantafyllopoulos, S.G. Neophytides, J. Catal. 239 (2006) 187–199.
[45] J.L.C. Fajín, M.N.D.S. Cordeiro, J.R.B. Gomes, J. Phys. Chem. C 116 (2012) 10120–10128.